# Large Eddy Simulations on the Flow Driven by a Rushton Turbine

**Jos Derksen and Harry E. A. Van den Akker**
Kramers Laboratorium voor Fysische Technologie, Delft University of Technology, 2628 BW Delft, The Netherlands

*Large eddy simulations were performed on the flow in a baffled stirred tank, driven by a Rushton turbine at $Re = 29{,}000$. The simulation procedure consisted of a lattice−Boltzmann scheme for discretizing the Navier−Stokes equations, and a force-field technique for representing the action of the impeller on the fluid. The subgrid-scale model was a conventional Smagorinsky model with a Smagorinsky constant $c_s = 0.12$. The uniform, cubic computational grid had a size of about $6 \times 10^6$ nodes. The computer code was implemented on a parallel, shared-memory computer platform. The results on the phase-resolved average flow, as well as on the turbulence characteristics, are compared with phase-resolved experimental data. The trailing vortex structure in the vicinity of the impeller was well represented by the simulations.*

## Introduction

The flow structures in a turbulently stirred tank are highly three-dimensional and complex, and cover a wide range of spatial and temporal scales. The fluid is circulated through the tank under the action of a revolving impeller. Baffles along the perimeter of the tank prevent the liquid from performing a solid-body rotation and, as a result, enhance mixing. In the wakes behind the blades of the impeller, three-dimensional vortices are formed (Yianneskis et al., 1987; Schäfer et al., 1998). These vortices, which retain their coherency over a significant distance into the bulk of the tank, are associated with high shear rates and strong turbulent activity. Therefore, they are essential to the mixing performance of the flow field.

A significant research effort has been invested in the description and the understanding of the flow phenomena encountered in a stirred tank. The global flow field can be characterized by its power requirements, the pumping capacity of the impeller, and (connected to the latter) the circulation time through the tank. In modern chemical engineering, however, there is a demand for local flow information with a view to optimizing mixing processes. On top of that, in many applications the rate-limiting phenomena take place at the small scales. For instance, droplet breakup is controlled by the shear rates at the scale of the drop size and the kinetic energy contained in this scale (Zhou and Kresta, 1998); in crystallizers, the flow around the particles strongly affects agglomeration (Smoluchowski, 1917); a major parameter in micromixing is the rate at which turbulent kinetic energy is dissipated at the flow's microscale (Bakker, 1996).

Detailed measurement techniques, such as laser Doppler anemometry (LDA), particle image velocimetry (PIV), and laser-induced fluorescence (LIF) have great significance in resolving large-scale as well as small-scale flow structures. The parameters dominating the smallest scales (energy dissipation rates, spectral information at the microscale, shear rates), however, are hardly accessible for these techniques. Essentially, computational modeling of the flow is an alternative route of describing stirred-tank flow, including its microscales. As many industrially relevant flows are associated with high Reynolds numbers, the scales corresponding to the high-frequency end of the spectrum cannot be resolved explicitly by numerical simulation. As a consequence, some way of turbulence modeling is necessary.

One of the options in this field is the technique of large eddy simulation (LES). In LES, the flow field is explicitly solved at the scales larger than (twice) the grid spacing (and than the time step for the temporal scales). At the subgrid-scale level, relatively simple turbulence modeling is applied,

Correspondence concerning this article should be addressed to J. Derksen.

as the turbulence at this scale is assumed to behave more or less universally, that is, independent of the flow geometry. In the case of flows with unsteady boundary conditions, such as the flow in a stirred tank, LES can be effectively employed to explicitly resolve the phenomena directly related to the unsteady boundaries. This technique contrasts with solving the Reynolds-averaged Navier–Stokes (RANS) equations in combination with a closure model for the Reynolds stresses. In the latter approach, it is unclear which part of the fluctuations (in terms of energy content as well as spectral distribution) is explicitly resolved, and which part is represented by the Reynolds stresses. The computational effort in LES is, however, significant. In contrast to RANS, no reduction of the computational domain as a result of symmetry properties of the geometry can be applied, that is, the full flow field needs to be modeled. In the second place, a fine grid is required to allow simple turbulence modeling at the subgrid-scale. Finally, meaningful flow statistics can only be extracted if the flow is calculated over a sufficiently long time span (covering several integral time scales). For a stirred tank, this means that the flow field needs to be simulated over several impeller revolutions.

Eggels (1996) was the first to report on LES in a stirred-tank configuration. The results are impressive. The snapshots of the flow field, presented in his article, give an unprecedented view of the turbulent flow structures in the tank. The agreement with experimental data was good. In the article, however, only a comparison with phase-averaged velocity measurements was made. In the vicinity of the impeller, the most interesting flow details, such as the trailing vortex structures, can only be revealed through phase-resolved data. In the work reported in the present article, the simulation procedure introduced by Eggels (1996), which consisted (next to the LES approach to turbulence) of a lattice–Boltzmann discretization scheme and a force-field algorithm for representing the revolving impeller, is extended with a more refined forcing algorithm. In addition, the flow in the vicinity of the impeller, as resolved by the simulations, is extensively described and compared with detailed, phase-resolved LDA experiments carried out in our laboratory (see Derksen et al., 1998).

In the next section, the flow geometry is defined. Then, the simulation procedure is presented. This is basically the same procedure as employed by Eggels (1996), and consists of three ingredients. First, a lattice–Boltzmann scheme for discretizing the incompressible Navier–Stokes equations. This scheme was chosen because of its computational efficiency, especially on parallel computer platforms. Second, a large eddy approach was chosen for the purpose of turbulence modeling. Third, an adaptive force-field procedure was used for describing the action of the impeller on the flow. The latter algorithm allows for imposing velocity boundary conditions in any point (not necessarily a grid point) within the flow domain. In the presentation of the results, the emphasis is on the region close to the impeller.

## Flow Geometry

Before we treat the setup of the simulations, the flow geometry is introduced. A view of both the tank and the impeller, as used in this research, is given in Figure 1. This geometry more or less represents a research standard, for which quite a few experimental as well as numerical data are available. The Reynolds number, which fully characterizes the flow system, is traditionally defined as $Re = ND^2/\nu$, with $N$ the impeller's rotational speed (in rev/s), $D$ the impeller diameter, and $\nu$ the kinematic viscosity of the working fluid. Note that four baffles are placed at the perimeter of the tank, and that the top level is a free surface. The axial level $z = 0$ corresponds with the impeller disk plane.

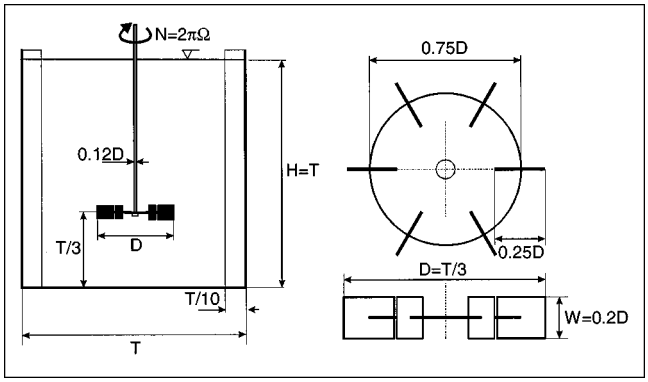


**Figure 1. Flow geometry.**

The tank (left) is equipped with four baffles to prevent solid body rotation of the fluid. At the top level there is a free surface. The impeller (right) is a Rushton turbine. The thickness of the disk and the impeller blades amounted to $0.017 \cdot D$.

## Simulation Procedure

### *Lattice–Boltzmann scheme*

The lattice–Boltzmann method provides an efficient Navier–Stokes solver. The basic idea is that fluid flow, which is governed by the laws of conservation of mass and momentum, can be simulated by a many-particle system obeying the same conservation laws (Frisch et al., 1986). In the lattice–Boltzmann approach to fluid flow, the particles reside on a lattice and are allowed to move from one site to the other during time steps. The collisions at lattice sites have to conserve mass and momentum.

Formally, the evolution of the many-particle system can be written in terms of the lattice–Boltzmann equation (Somers, 1993)

$$N_i(x + c_i,\, t+1) = N_i(x,t) + \Gamma_i(N), \qquad (1)$$

with $N_i$ the mass of a particle traveling with velocity $c_i$, and $\Gamma_i$ the collision operator that depends in a nonlinear way on all particles involved in the collision. The differential form of Eq. 1 can be derived from a first-order Taylor expansion of the term at the lefthand side:

$$\frac{\partial N_i}{\partial t} + c_{i\alpha}\frac{\partial N_i}{\partial x_\alpha} = \Gamma_i(N), \qquad (2)$$

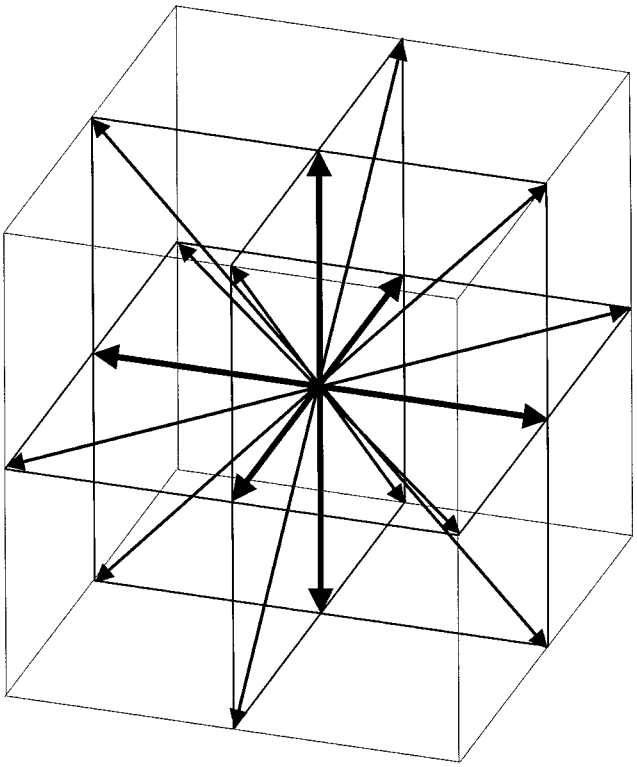

**Figure 2. Velocity directions $c_i$ (18) of the FCHC lattice projected on 3-D space.**

The vectors in bold face have unit length and a multiplicity $m_i = 2$; the vectors in light face have a length of $\sqrt{2}$ and a multiplicity $m_i = 1$.

with a summation over the repeated Greek index. The velocity directions $c_i$ form a discrete set, as the particles are only allowed to travel to neighboring lattice sites during a single time step. A lattice that is commonly applied for simulation of the Navier–Stokes equations (Somers, 1993) is a three-dimensional projection of a four-dimensional face-centered hypercube (FCHC) (see Figure 2). The projected lattice has 18 velocity directions. Due to the projection, each direction is associated with a multiplicity parameter $m_i$, as indicated in Figure 2. The symmetry properties of the lattice are summarized in the Appendix. The collision operator has to obey mass and momentum conservation:

$$\Sigma_i \Gamma_i(N) = 0 \tag{3}$$

$$\Sigma_i c_{i\alpha} \Gamma_i(N) = f_\alpha, \tag{4}$$

with $f$ an external force, applied to the flow. The mass density $\rho$ and the momentum concentration $\rho u$ are related to $N_i$ and $c_i$ according to

$$\rho = \Sigma_i N_i \tag{5}$$

$$\rho u_\alpha = \Sigma_i c_{i\alpha} N_i. \tag{6}$$

Note that all flow variables presented are dimensionless. The unit of length is the lattice spacing, the unit of time is the time needed for the particles to travel a single lattice spacing, and the unit of mass is related to the (initially uniform) mass per lattice cell.

A summation over all directions $i$ of Eq. 2 and application of the mass conservation constraint on $\Gamma_i$ (Eq. 3) yield the continuity equation:

$$\frac{\partial \rho}{\partial t} + \frac{\partial \rho u_\alpha}{\partial x_\alpha} = 0. \tag{7}$$

If $N_i$ is written in terms of density, momentum concentration, and stress (see Eggels and Somers, 1995) according to:

$$N_i = \frac{m_i \rho}{24}\left\{1 + 2c_{i\alpha} + 3c_{i\alpha}c_{i\beta}u_\alpha u_\beta - \frac{3}{2}u_\alpha^2 - 6\nu\left[c_{i\alpha}\frac{\partial c_{i\beta}u_\beta}{\partial x_\alpha} - \frac{1}{2}\frac{\partial u_\alpha}{\partial x_\alpha}\right]\right\}, \tag{8}$$

a substitution into Eq. 2 multiplied by $c_{i\alpha}$, followed by a summation over all velocity directions $i$, and a proper use of the symmetry relations of the FCHC lattice (Appendix), yield

$$\frac{\partial \rho u_\alpha}{\partial t} + \frac{\partial \rho u_\alpha u_\beta}{\partial x_\beta} = -\frac{\partial p}{\partial x_\alpha} + \frac{\partial}{\partial x_\beta}\left[\nu\rho\left(\frac{\partial u_\beta}{\partial x_\alpha} + \frac{\partial u_\alpha}{\partial x_\beta}\right)\right] - \frac{1}{2}\frac{\partial}{\partial x_\alpha}\left(\nu\rho\frac{\partial u_\beta}{\partial x_\beta}\right) + f_\alpha. \tag{9}$$

For the pressure $p$, the following equation of state applies

$$p = \frac{1}{2}\rho\left[1 - \frac{1}{2}u_\alpha u_\alpha\right]. \tag{10}$$

In the incompressible limit, Eq. 9 corresponds to the Navier–Stokes equation. The collision operator $\Gamma_i$ can be specified by substituting Eq. 8 into Eq. 2:

$$\Gamma_i(N) = \frac{m_i \rho}{12}\left[c_{i\alpha}\frac{\partial c_{i\beta}u_\beta}{\partial x_\alpha} - \frac{1}{2}\frac{\partial u_\alpha}{\partial x_\alpha}\right] + \frac{m_i}{12}c_{i\alpha}f_\alpha. \tag{11}$$

The evolution of the flow in time is now simulated as follows. At a specific moment, the flow field is fully defined by the discrete field of particle masses $N(x, t)$. In the first phase of a time step (the propagation phase), the particles move to their neighboring sites, that is,

$$N_i^{\mathrm{I}}(x,t) = N_i(x - c_i, t-1). \tag{12}$$

Then, by means of the inverse of Eq. 8, the $N_i^{\mathrm{I}}(x,t)$ field is transformed into a field in terms of the (common) flow variables such as density, velocity, force, and stress. The collision operator (Eq. 11) is applied to this transformed field. After the collision, the field is transformed back to the $N_i(x,t)$ field,

and the system is ready for the next time step. By tuning the impact of the collision operator on the higher-order terms, the lattice–Boltzmann discretization scheme can be given third-order accuracy in space and time (Eggels and Somers, 1995).

In the propagation phase as well as in the collision phase, boundary conditions can be established. In the propagation phase this is done by imposing rules for mass densities leaving and entering the domain (e.g., a no-slip wall is a wall on which mass densities bounce back). During collisions, an external force field can be calculated in such a way that the flow is forced to prescribed velocities at specific positions within the flow domain. The latter approach was adopted for modeling the revolving impeller and the cylindrical tank wall (including the baffles). It will be discussed in more detail in a later section.

The major reasons for employing a lattice–Boltzmann discretization scheme are its almost full locality of operations, its computational efficiency (in terms of floating-point operations per lattice site and time step), and its ability to simulate flows in complex geometries. As a consequence of the first reason, the scaling properties of the scheme are almost ideal: a grid refinement with a factor of 2 in all three dimensions leads to a factor of 8 in storage requirements and a factor of 16 in run time (the lattice–Boltzmann scheme is an explicit scheme; a spatial refinement requires a reduction of the physical time step as well). Furthermore, parallelization of the computer code by means of domain decomposition is relatively simple: only the propagation phase needs communication between the processors. During this phase, the processors exchange particles that cross subdomain boundaries.

### *Large eddy simulation*

A direct simulation of stirred-tank flow at industrially relevant Reynolds numbers ($Re \geq 10^4$) is not feasible, as the resolution of all length and time scales in the flow would require enormous amounts of grid cells and time steps. However, the small scales in the flow can be assumed to be universal and isotropic, that is, independent of the specific flow geometry. As a result, they can be modeled with relative ease. In a large eddy simulation (LES), the range of resolved scales is reduced by filtering out the small scales. The effect the small scales have on the larger scales is taken into account with a subgrid-scale model. In this research, a standard Smagorinsky model (Smagorinsky, 1963) was used. This is an eddy viscosity model with a subgrid-scale eddy viscosity ($\nu_t$) that is independent on the local, resolved deformation rate:

$$\nu_t = \lambda_{\text{mix}}^2 \sqrt{S^2}, \tag{13}$$

with $\lambda_{\text{mix}}$ the mixing length of subgrid-scale motion and $S^2$ the resolved deformation rate:

$$S^2 = \frac{1}{2}\left(\frac{\partial u_\alpha}{\partial x_\beta} + \frac{\partial u_\beta}{\partial x_\alpha} - \frac{2}{3}\delta_{\alpha\beta}\nabla\cdot u\right)^2, \tag{14}$$

with $\delta_{\alpha\beta}$ the Kronecker delta. In the standard Smagorinsky model, the ratio between the mixing length $\lambda_{\text{mix}}$ and the lattice spacing $\Delta$ is constant:

$$c_s = \frac{\lambda_{\text{mix}}}{\Delta}. \tag{15}$$

A value of 0.12 was adopted for $c_s$, which is within the range of values commonly used in shear-driven turbulence (Piomelli et al., 1988).

The implementation of the subgrid-scale model in the lattice–Boltzmann scheme is straightforward. In the collision phase, rather than the molecular viscosity $\nu$, now the total viscosity $\nu + \nu_t$ is used. The subgrid-scale model does not break down the locality of the collision operation, as the viscous stresses are contained within the solution vectors of the lattice–Boltzmann solver. As a result, we do not need to discretize the gradients contained in Eq. 14.

### *Impeller and tank wall treatment*

In its basic and most efficient form, the lattice–Boltzmann scheme employs a cubic, uniform lattice. In order to model nonsquare or moving objects in the flow domain, we have developed, within the lattice–Boltzmann framework, an adaptive force-field technique (Derksen et al., 1997) based on earlier work by Goldstein et al. (1993). The algorithm calculates forces acting on the flow in such a way that the flow field has prescribed velocities at points within the domain. In this way, the boundary conditions at the revolving impeller and at the cylindrical tank wall (including the baffles) were imposed.

The impeller and the tank wall are defined as a set of $M$ control points $r_j^{(n)}$ $(j = 1 \cdots M)$ on their surface, where the superscript $(n)$ indicates the moment in time. There is no restriction on the position of these points in the flow domain; they do not need to coincide with lattice sites. At the points on the impeller, we require a velocity equal to $w_j^{(n)} = \mathbf{\Omega} \times r_j^{(n)}$, with $\mathbf{\Omega}$ the angular velocity of the impeller ($|\mathbf{\Omega}| = 2\pi N$), whereas on the tank wall the required velocity is zero: $w_j^{(n)} = 0$.

The preceding demands can be achieved effectively through a control algorithm which, at each time step, determines the (interpolated) mismatch between the actual flow velocity and the prescribed flow velocity at the control points, and then adapts the force field in such a way that it suppresses the mismatch. The deviation between the actual and the prescribed velocity ($d_j^{(n)}$) is determined by a second-order interpolation of the flow velocities at the lattice sites:

$$d_j^{(n)} = w_j^{(n)} - \Sigma_k G_k\left(r_j^{(n)}\right) u_k^{(n)}, \tag{16}$$

where the sum is over the lattice sites in the vicinity of $r_j^{(n)}$, and $G_k$ are the interpolation coefficients. These coefficients also serve to distribute the forces that reduce the deviation $d_j^{(n)}$ over the lattice sites

$$f_k^{(n)} = f_k^{(n-1)} + q\Sigma_j G_k\left(r_j^{(n)}\right) d_j^{(n)}, \tag{17}$$

with $q$ a relaxation factor. The accuracy of the control algorithm can be improved by iterating Eqs. 16 and 17 a few times per time step. It should be noted that the force calculation breaks down the locality of the lattice–Boltzmann scheme, as it requires interpolation and distribution. As a result, in a parallel implementation, the forcing step needs communication over subdomain boundaries.

The forcing procedure offers great flexibility. A new impeller or tank design only needs a new set of surface points defining the geometry. There is no need for building a new computational mesh.

### *Practical aspects of the simulations*

A cubic computational grid of $180^3$ lattice cells was defined. At the walls of this cube, bounce-back boundary conditions were imposed, except for the top wall, where a free-slip boundary condition was set to mimic the free surface. Inside this computational domain, the cylindrical tank wall, the baffles, the impeller, and the shaft the impeller was mounted on, were defined by sets of points. The forcing algorithm described earlier takes care of the boundary conditions at these points. The diameter of the impeller amounted to 60 times the lattice spacing ($60 \cdot \Delta$), whereas the thickness of the impeller disk and blades was $\Delta$. The other dimensions of the impeller can be derived from Figure 1. The nearest-neighbor distance between the forcing points at the impeller surface was $0.7 \cdot \Delta$. The total number of points defining the impeller was 16,482. The diameter of the tank was $180 \cdot \Delta$. The baffles were defined with a thickness of $\Delta$. The total number of points on the tank wall was 152,920.

The angular velocity $\Omega$ of the impeller is limited mainly by the incompressibility condition. It has been explained before that only in the incompressible limit, that is, if $|u|^2 \ll 1$ (the speed of sound in the lattice–Boltzmann framework is of the order of one), the lattice–Boltzmann scheme converges toward the Navier–Stokes equations. In the current work $\Omega = 2\pi/1{,}600$, that is, the impeller makes a full revolution in 1,600 time steps. As a result, the tip speed, $v_{\text{tip}} = \Omega D/2$, of the impeller was 0.12 (in lattice units, i.e., lattice spacings per time step). In the simulations, the velocities in the tank did not exceed 0.22. The Reynolds number can be selected by the value of the kinematic viscosity. A Reynolds number of 29,000 (which was chosen because of the availability of experimental data, that is, Wu and Patterson, 1989; Derksen et al., 1998) requires a viscosity of $7.76 \times 10^{-5}$ (in lattice units).

The computer code for executing the simulations was implemented on an HP-Convex S-Class parallel computer, equipped with four processing units and a (shared) memory of 1 Gbyte. In order to keep the software portable to computer platforms with a distributed memory architecture, it was written according to the single-program, multiple-data (SPMD) paradigm, in which the same program simultaneously works on different data sets (in our case on different parts of the flow domain). Communication between the processing units was controlled by the PVM message-passing tool (Geist et al., 1994), which was embedded in the software. The memory requirements of the simulations are proportional to the grid size. On every grid node 21 (18 directions and 3 force components) single-precision, real values need to be stored (the memory requirements associated with the forcing points are relatively small). As a result, the program occupies approximately $180^3 \times 21 \times 4 \approx 0.5$ Gbyte of memory. When the code is running on all four processors in parallel, calculation of a single time step takes about 25 s (wall-clock time).

The simulations were started from a zero-velocity field on a relatively coarse grid ($120^3$ cells). After 20 impeller revolutions a more or less steady state was reached. This was checked by monitoring the velocity as a function of time in the upper part of the tank. Then the flow field was transferred to the $180^3$ grid by linear interpolation. It again took about 15 revolutions for the flow system to become (quasi-) steady. In a subsequent session of 25 revolutions, flow data were collected and statistically processed. As a result, the parallel computer was kept fully busy for almost a month.

## Results

### *Single realizations of the flow field*

Impressions of the flow field are given in Figure 3. The flow in a horizontal plane just below disk level is depicted in Figure 3a. Away from the impeller, the flow behaves erratically. Eddylike structures can be observed. Close to the impeller, the flow seems to be more coherent. The wakes behind the impeller blades can be clearly identified. Locally, velocities in the wakes are significantly higher than the impeller tip speed. The largest velocity encountered in Figure 3a amounts to almost $2 \cdot v_{\text{tip}}$. Note the minor flow outside the tank, which is induced by the force field that takes care of the boundary conditions at the tank wall. A detail of the same flow field, relative to the impeller, is shown in Figure 3b. Immediately behind the impeller blade, fluid is strongly forced into the radial direction. No-slip boundary conditions were imposed at the impeller blade. The velocity field shown in Figure 3b demonstrates the ability of the adaptive force field to satisfy this boundary condition.

In a vertical plane in the impeller stream (Figure 3c), a strong radial outflow along with trailing vortices are observed. The latter are formed in the wakes of the blades and then swept into the tank, where they keep their identity over a significant radial distance. In Figure 3c, the upper and lower vortices associated with the two most recent blade passages can be identified.

The temporal behavior of the flow strongly depends on the position in the tank. The radial velocity as a function of time at three typical positions is depicted in Figure 4. At the impeller tip (Figure 4a), most of the fluctuations are periodic as the result of the regular blade passage. Further away from the impeller (Figure 4b), the fluctuations become less coherent. At the same time, the pdf shows a less detailed structure. In the bulk of the tank (Figure 4c), fluctuations are relatively weak and have low frequencies.

### *Phase-averaged results: Comparison with experiments*

The current stirred-tank geometry, operated under turbulent conditions, has been studied experimentally in quite some detail. In the more recent studies, LDA was used to locally measure the flow velocity with high spatial and temporal resolution (see, e.g., Wu and Patterson, 1989; Stoots and Cal-

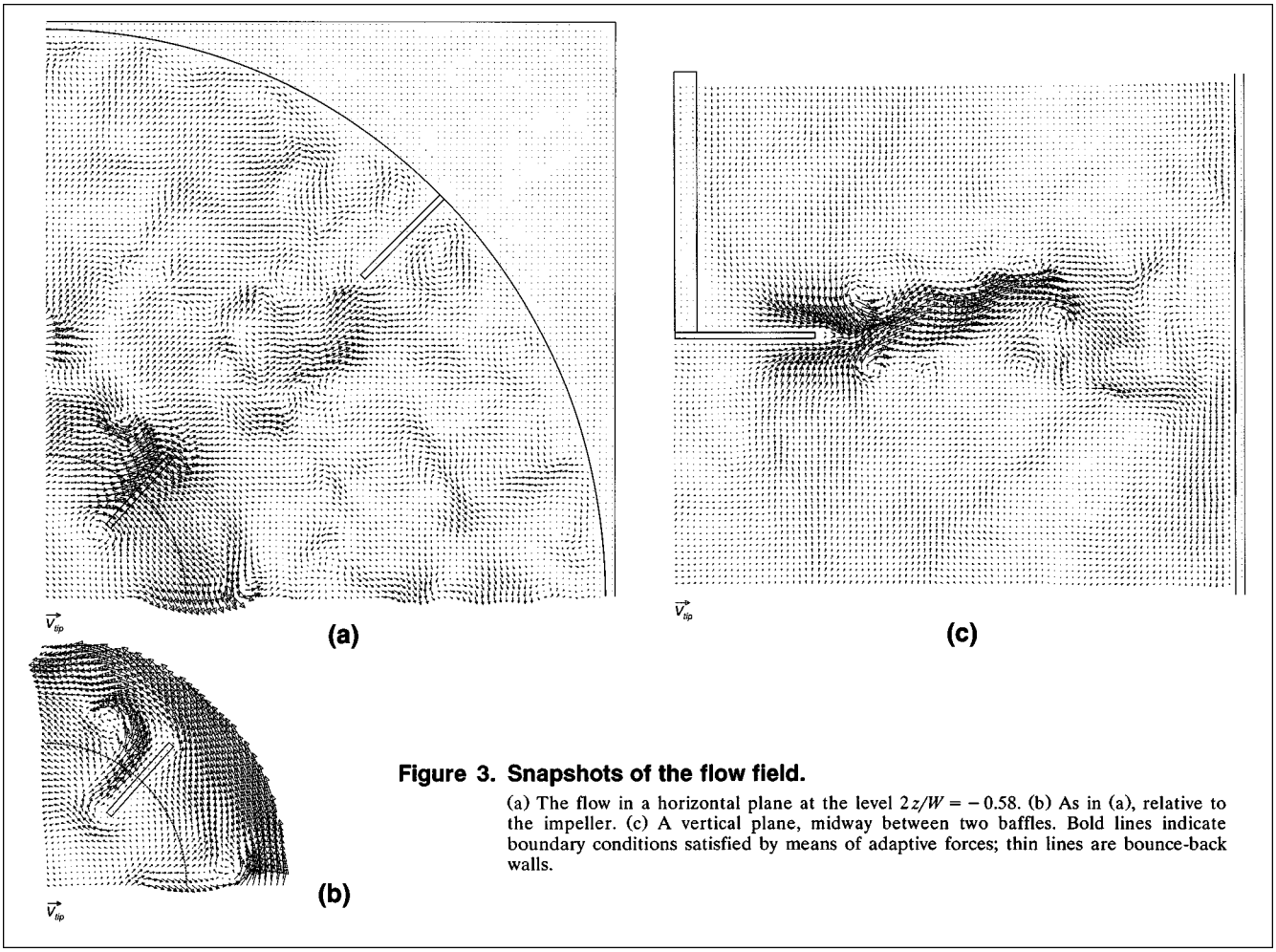


**Figure 3. Snapshots of the flow field.**

(a) The flow in a horizontal plane at the level $2z/W = -0.58$. (b) As in (a), relative to the impeller. (c) A vertical plane, midway between two baffles. Bold lines indicate boundary conditions satisfied by means of adaptive forces; thin lines are bounce-back walls.

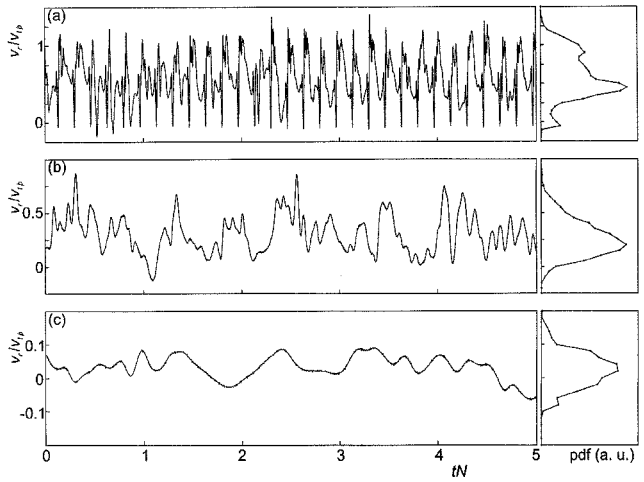


**Figure 4. Traces of the radial velocity component as a function of time (left), and the corresponding probability density functions (PDFs) (right).**

The PDFs were determined over 25 impeller revolutions. They are in arbitrary units. (a) At the position $2z/W = 0.1$, $2r/D = 1.0$. (b) At $2z/W = 0.1$, $2r/D = 2.4$. (c) At $2z/W = 14.9$, $2r/D = 1.0$. Note the different velocity scales.

abrese, 1995). A distinction between phase-resolved and phase-unresolved experiments needs to be made. In phase-resolved experiments the position of the impeller is recorded along with every individual velocity measurement. This allows for a reconstruction of the mean flow field and its fluctuations as a function of the impeller angle. Information on the angle of the impeller is not contained in phase-unresolved experiments. In the latter case, only phase-averaged data can be extracted.

An extensive, phase-averaged data set has been reported by Wu and Patterson (1989). They have presented, among other things, axial profiles in the impeller outstream of the mean and RMS values of the three velocity components at various radial distances from the impeller tip. Their measuring volume was located in a plane midway between two baffles. The Reynolds number was the same as in the current study: $Re = 29{,}000$. Furthermore, Derksen et al. (1998) performed detailed three-dimensional, phase-resolved LDA experiments under flow conditions that closely resemble Wu and Patterson's.

In Figure 5, phase-averaged results on the mean radial and tangential velocity obtained by measurement and simulation are compared. The well-known radial discharge flow is pre-

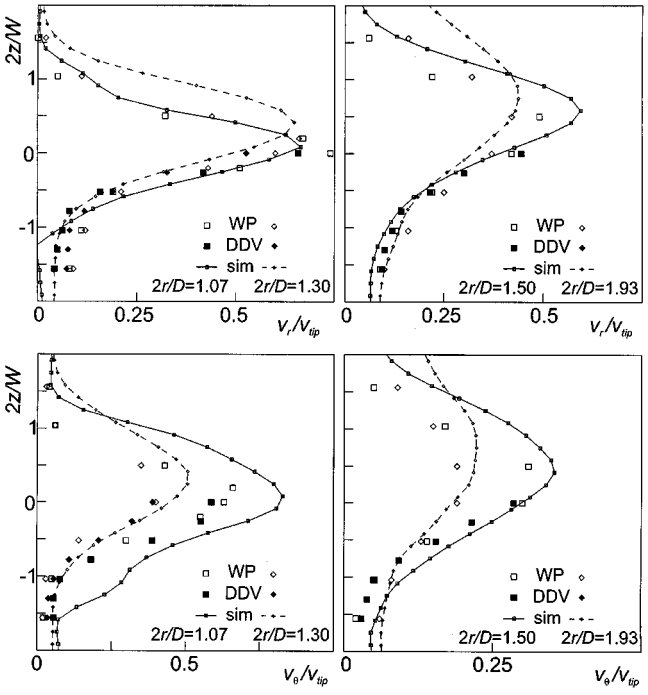


**Figure 5. Axial profiles of the phase-averaged radial and tangential velocity components in the impeller outstream.**

Comparison between simulations and experiments (WP corresponds to Wu and Patterson, 1989; DDV to Derksen et al., 1998).

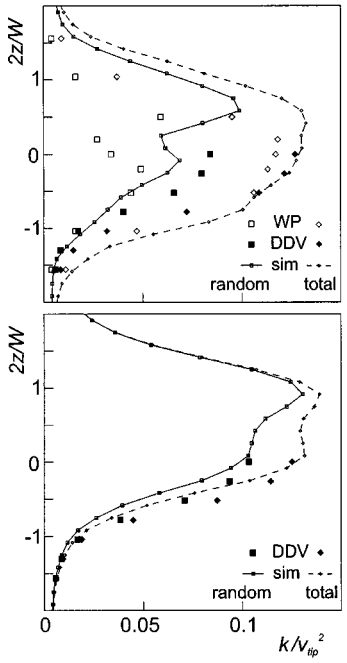


**Figure 6. Axial profiles of the kinetic energy.**

Top: $2r/D = 1.07$; bottom: $2r/D = 1.3$. A distinction between the total kinetic energy and the random kinetic energy is made. Comparison between simulations and experiments (WP corresponds to Wu and Patterson, 1989; DDV to Derksen et al., 1998).

dicted with a fair level of accuracy by the simulations. The correspondence between experiment and simulation with respect to the maximum radial velocity as a function of the radial position is good, whereas the maximum tangential velocities are overestimated by the simulations by some 15%. The spreading rate of the discharge flow is overestimated as well. More fluid from the bulk of the tank is entrained into the discharge flow than in real life, especially above the disk.

The deviations observed might be caused by (still) a lack of spatial resolution. A crude estimate of the wall friction velocity (see, e.g., Hinze, 1975) at the impeller blades shows that the lattice spacing corresponds to some 75 wall units, which is insufficient to fully resolve the boundary layers at the blades. Another reason might be neglect of the presence of solid walls in the subgrid-scale model. In, for example, pipe flow simulations (Eggels, 1994) it is well known that, due to the suppression of turbulence near the wall, the eddy-viscosity needs to be reduced near the wall to get good agreement with experiments. Application of wall functions at the impeller blades and disk will therefore probably reduce both the strength, and the width of the radial impeller outflow. With the introduction of wall functions, however, more empiricism is introduced.

Velocity fluctuations in a turbulently stirred tank are partly periodic (directly related to the blade passage frequency; see also Figure 4), partly random (turbulence). As a result, the kinetic energy contained in the velocity fluctuations can be divided into a random part and a coherent part. Sometimes the coherent contribution to the kinetic energy is presented as pseudoturbulence (Van 't Riet and Smith, 1975). The relative strength of both contributions can easily be identified in a phase-resolved measurement system. The *total* kinetic energy in the velocity fluctuations is

$$k_{\text{tot}} = \frac{1}{2}\left(\overline{u_i^2} - \overline{u_i}^2\right), \tag{18}$$

with $u_i$ the $i$th velocity component. Note the summation convention over the repeated index $i$. The averages are over all velocity samples, irrespective of the angular position of the impeller. The random part of the kinetic energy can be determined if angle-resolved average data are available:

$$k_{\text{ran}} = \frac{1}{2}\left(\overline{\langle u_i^2\rangle_\theta - \langle u_i\rangle_\theta^2}\right), \tag{19}$$

with $\langle\ \rangle_\theta$ the average value at the angular position $\theta$. In Eq. 19, the overbar denotes averaging over all angular positions. The energy in the coherent fluctuations is found by subtracting $k_{\text{ran}}$ from $k_{\text{tot}}$. The distinction between random and coherent kinetic energy was also made by Wu and Patterson (1989). However, they divided the kinetic energy into random and coherent by means of a fitting procedure on the autocorrelation function of the velocity signal, as they had no phase-resolved data at their disposal.

In Figure 6, the axial profiles of $k_{\text{ran}}$ and $k_{\text{tot}}$, extracted from the simulations, are compared with the experimental data by Wu and Patterson (1989) and Derksen et al. (1998). First, we note that the random kinetic energy at $2r/D = 1.07$

deviates significantly between both experimental data sets. This is most likely due to the different procedures for dividing random and coherent fluctuations. The simulated maximum levels of kinetic energy correspond well with the experimental data. As in the average velocity data (Figure 5), the width of the axial profiles is overestimated by the simulations, especially at the upper side of the impeller disk. The spatial distribution of the kinetic energy in the impeller outstream is discussed in more detail in the next section.

In LES, only part of the fluctuations is resolved by the grid. The part that resides on the subgrid scales is modeled in terms of an eddy viscosity (Eq. 11). In the profiles presented in Figure 6, less than 0.1% of the kinetic energy is at a subgrid-scale level.

### *Phase-resolved flow fields: Comparison with experiments*

An important flow phenomenon, which can only be observed in a frame of reference that moves with the impeller, is the trailing vortex system. It develops in the wake of a turbine blade, and is then advected by the impeller stream into the bulk of the tank. With the vortex structure, high levels of turbulent activity and high velocity gradients are associated (Lee and Yianneskis, 1998). Therefore, this structure plays an important role in the mixing capability of the stirred tank. Trailing vortices have been reported in many experimental studies, but, to the best of the authors' knowledge, they are never treated comprehensively in a numerical study on stirred-tank flow.

Phase-resolved, mean flow fields in the vicinity of the impeller are shown in Figure 7 at various angles with respect to an impeller blade. For comparison, the experimental data by Derksen et al. (1998) are given as well. Qualitatively as well as quantitatively, the agreement between the simulated and measured flow field is good. The radial impeller outflow is directed slightly upward, and, as a result, exhibits an asymmetry with respect to the plane of the impeller disk. The lower trailing vortex can be easily identified, whereas the upper vortex is visible, albeit in a less pronounced way. The vortex core below the disk is closer to the impeller disk plane (approximately at $2z/W = -0.35$ in the simulated field), compared to the upper vortex ($2z/W \approx 1.0$). In addition the radial positions of the upper and lower vortex differ.

Yianneskis et al. (1987) proposed characterizing the curve along which the trailing vortex is swept into the tank, by connecting the points in a horizontal plane where the mean axial velocity component equals zero. In their study, they focused on the upper vortex, which was seen to move almost horizon-

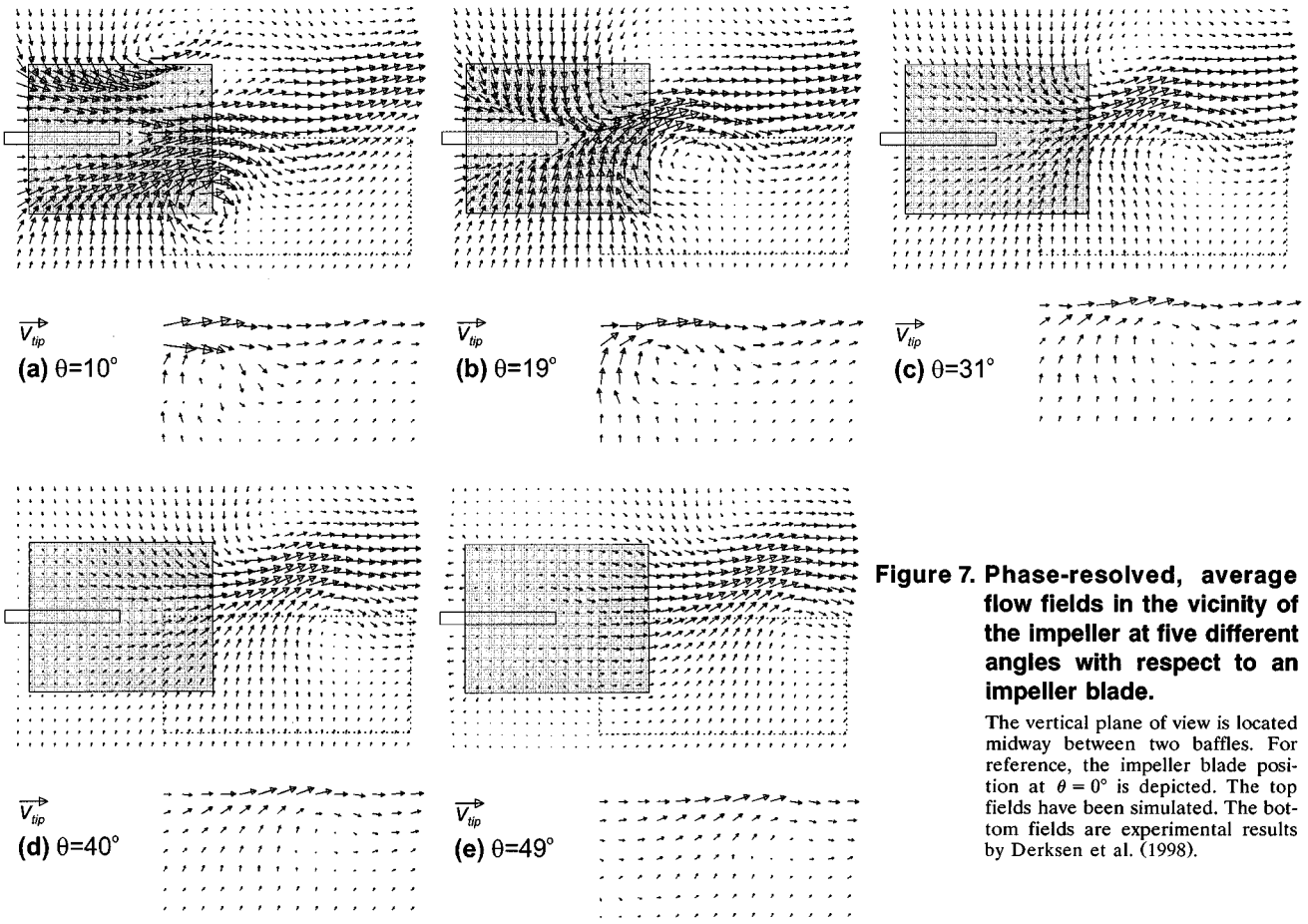


**Figure 7. Phase-resolved, average flow fields in the vicinity of the impeller at five different angles with respect to an impeller blade.**

The vertical plane of view is located midway between two baffles. For reference, the impeller blade position at $\theta = 0°$ is depicted. The top fields have been simulated. The bottom fields are experimental results by Derksen et al. (1998).

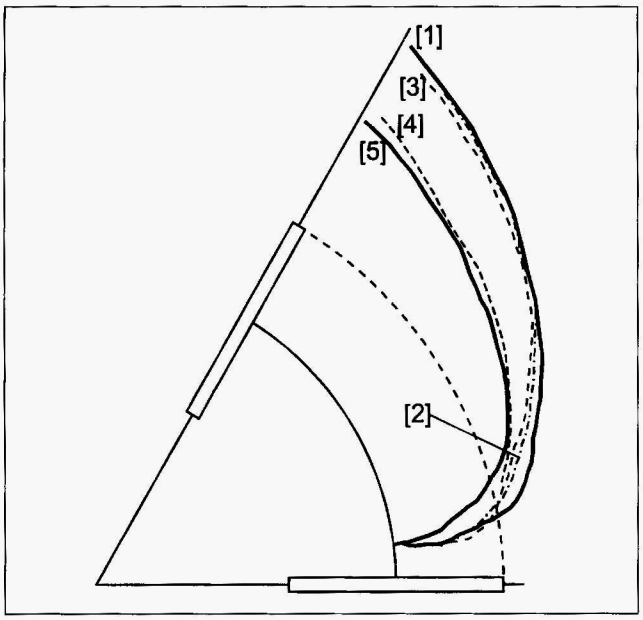


**Figure 8. Projections of the position of the vortex core on a horizontal plane as found in various studies.**

[1] This work in the plane $2z/W = -0.35$. [2] From Stoots and Calabrese (1995), measured underneath the disk. [3] From Derksen et al. (1998), measured underneath the disk. [4] From Yianneskis et al. (1987), measured above the disk. [5] This work in the plane $2z/W = 1.0$.

tally in the $2z/W = 1.0$ plane. Stoots and Calabrese (1995) mainly studied the lower vortex and observed its core to move slightly downwards, starting close behind the blade at $2z/W \approx -0.5$, whereas at $\theta = 60°$ it was at $2z/W \approx -1.2$. Finally, the experimental results in Figure 7 (Derksen et al., 1998) show a vortex core moving approximately horizontally in the $2z/W = -0.5$ plane. In Figure 8, the vortex core paths derived from the three experimental studies mentioned earlier are compared to the simulated paths. The results of the simulations on the lower vortex agree very well with the experimentally determined lower vortex path. The same applies for the upper vortex.

The trailing vortex core is associated with high levels of turbulent kinetic energy, as can be seen in Figure 9. The vortex paths almost coincide with (lower vortex), or are near to (upper vortex) the regions of highest turbulent kinetic energy. In Figure 10, the same radial-axial planes as in Figure 7 were chosen to plot the turbulent kinetic energy, that is, $1/2(\langle u_i^2 \rangle_\theta - \langle u_i \rangle_\theta^2)$. It can be concluded that the simulations resolve very well the structure of the turbulent kinetic energy field as well as the levels of kinctic energy.

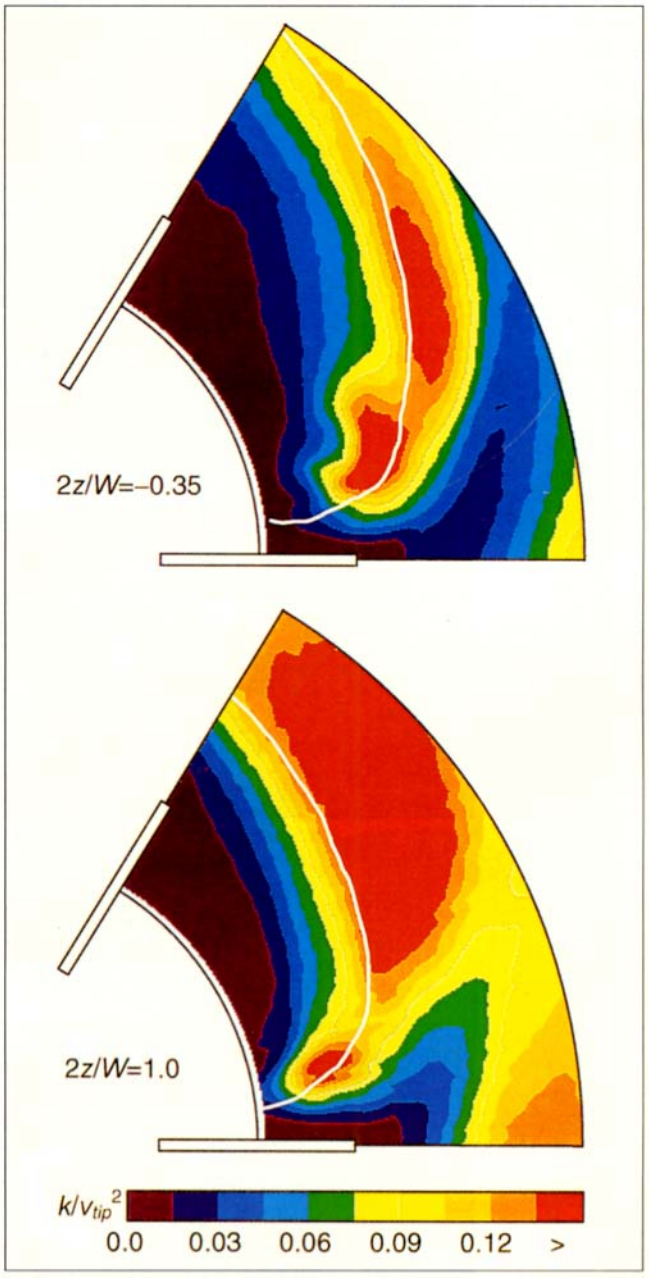


**Figure 9. Contours of the turbulent kinetic energy in the planes the trailing vortex cores move in; the curves represent the paths of the vortex cores.**

### *Energy dissipation*

The energy dissipation rate ($\epsilon$) is of relevance for many mixing applications, as it controls the flow at the microscale. At the same time, it is hardly possible to directly measure the dissipation rate (a very sophisticated attempt, based on 3-D laser-induced fluorescence, was undertaken by Dahm et al. 1991). Indirect ways of measuring $\epsilon$ include measuring turbulence intensities and length scales (through, e.g., LDA). The assumptions about the nature of the turbulence (among others, isotropy) needed to derive the dissipation rates from the measured quantities are, however, not very appropriate in stirred-tank flow. Since the kinetic energy field is estimated accurately by the simulations, at least in the impeller outflow region, we are confident that the simulations can predict the energy dissipation rate with acceptable accuracy.

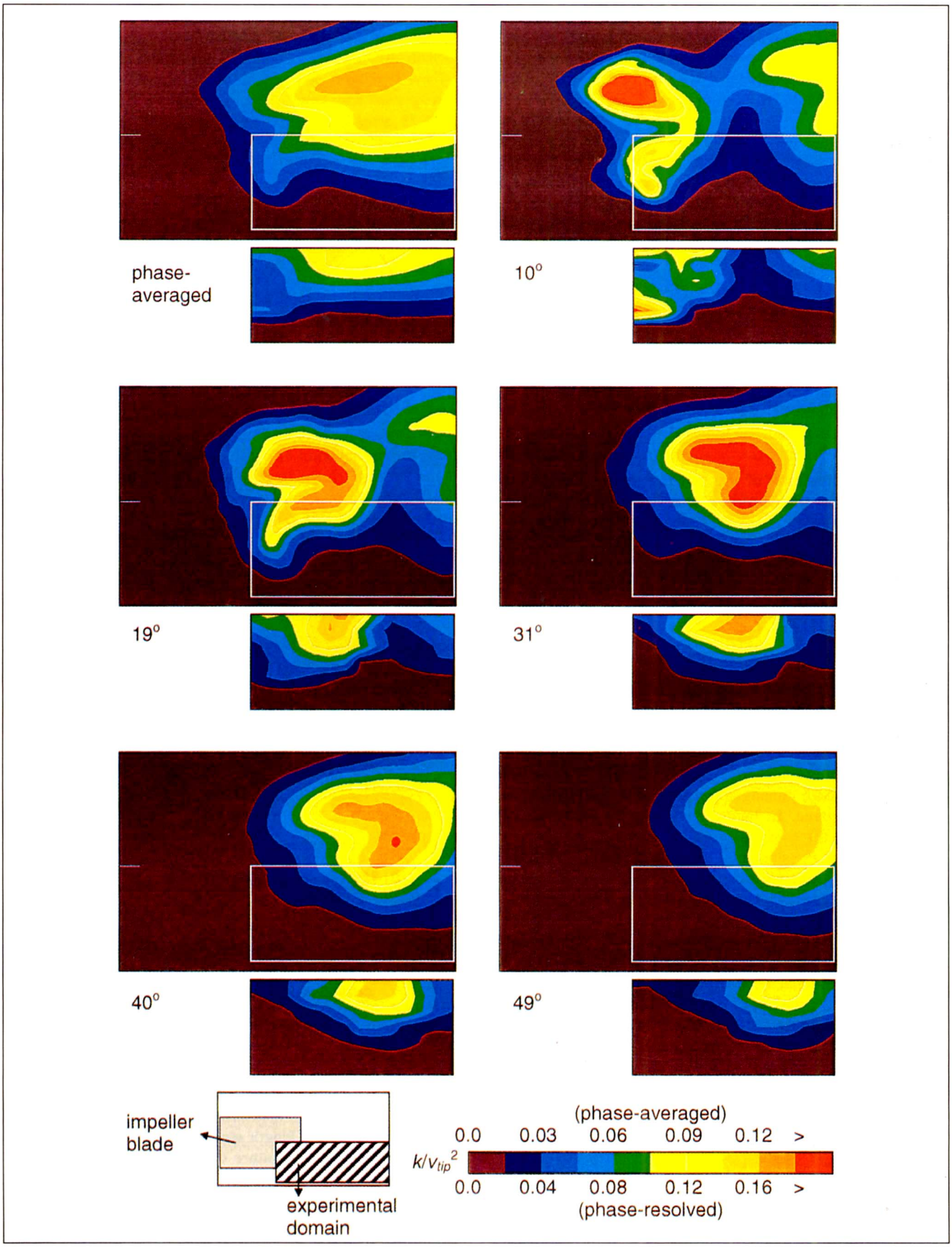


**Figure 10. Measured vs. simulated turbulent kinetic energy fields in various vertical planes.**

The plane is located midway between two baffles. The position with respect to an impeller blade is indicated at the bottom of the figure.

The dissipation rate distribution throughout the tank is very inhomogeneous (see Figure 11). Energy dissipation is concentrated in the impeller swept region and in the impeller outflow. Dissipation rates encountered in the tank cover a range of more than three decades. The total consumed power in the tank is determined by the torque and the angular speed of the impeller. The torque can be deduced from the adaptive force field, which represents the action of the impeller on the fluid. This way, a power number, defined as

$$Po = \frac{T\Omega}{\rho N^3 D^5}, \tag{20}$$

(with $T$ = torque) equal to 5.7 is found. Experiments (Rushton et al., 1950; Distelhoff et al., 1995) show values in the range $Po = 4.6, \ldots, 5.9$ at $Re \approx 30{,}000$. As a consequence, the region labeled red in Figure 11, that is, the region with $\epsilon/D^2N^3 > 4.6$ has a dissipation rate some seventeen times the average dissipation rate. If the tank is divided into three domains [i.e., the impeller swept volume ($2r/D \le 1$ *and* $|2z/W| \le 1$); the impeller outflow region ($2r/D > 1$ *and* $|2z/W| \le 2$); and the rest of the tank], the dissipated power in the respective domains amounts to 18, 60, and 22% of the total dissipated power.

The way energy dissipation evolves in the impeller swept region is depicted in Figure 12. Very high dissipation rates (locally exceeding 100 times the tank-average value) are encountered at the blade edges and in the near wake of the blades. With increasing angle with respect to the blades, the dissipation rapidly drops.

## Conclusions

In this article, we have investigated the potential of large eddy simulations for the highly complex flow in a stirred tank, driven by a Rushton turbine at $Re = 29{,}000$. Obviously, this type of simulation requires a large computational effort, in terms of computer time as well as memory access. The only way to keep the computational cost within a more or less acceptable level was to exploit an efficient numerical scheme. The lattice–Boltzmann procedure, as introduced by Eggels (1996) for this purpose, has proven its efficiency. It can be implemented easily on parallel computer platforms and, because of the locality of its operations, almost no computational overhead arises. Furthermore, the adaptive force-field technique for imposing the impeller and tank-wall boundary conditions does not reduce the scheme's efficiency. At the same time, the adaptive force-field technique makes the simulation procedure suitable for geometry optimization studies. By simply changing the sets of points defining the impeller and tank wall, geometrical adaptations can be made, and their effect on the flow, including the turbulence characteristics, can be studied.

In the flow system at hand, the LES approach to turbulence has advantages over application of closure models for the Reynolds stresses in the Reynolds-averaged Navier–Stokes equations. In the first place, the Smagorinsky subgrid-scale model contains a single, semiempirical parameter ($c_s$ in Eq. 15), whereas typically five to ten parameters (which have to be empirically tuned in relatively simple flow systems) are required for closure models. More importantly, however, is the clear (spectral) distinction between resolved and unresolved scales in LES by the grid spacing. We feel that the latter contributed to the good resolutions of the trailing-vortex system.

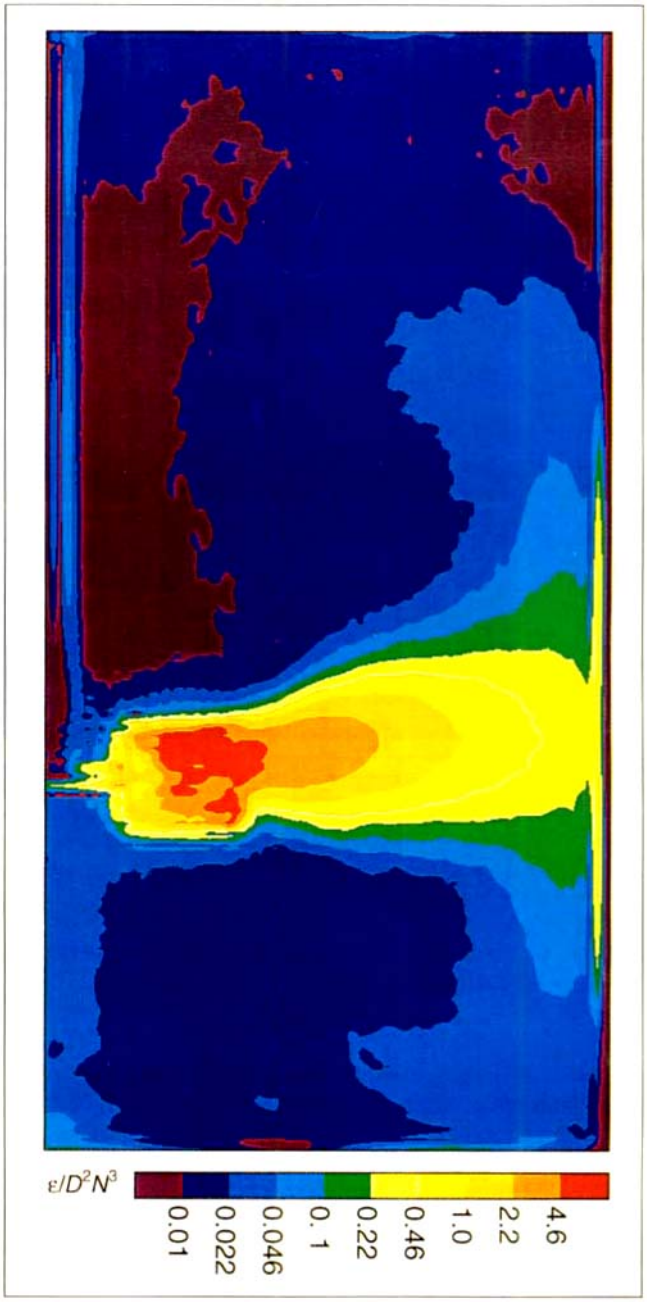


**Figure 11. Phase-averaged energy dissipation rate in a vertical plane, located midway between two baffles.**

Good agreement with experimental data is, of course, vital to any simulation procedure. Phase-resolved velocity fields as well as turbulent kinetic-energy levels were well predicted by the simulations. Particularly the vortex core paths, both above and below the impeller disk, were predicted correctly. The

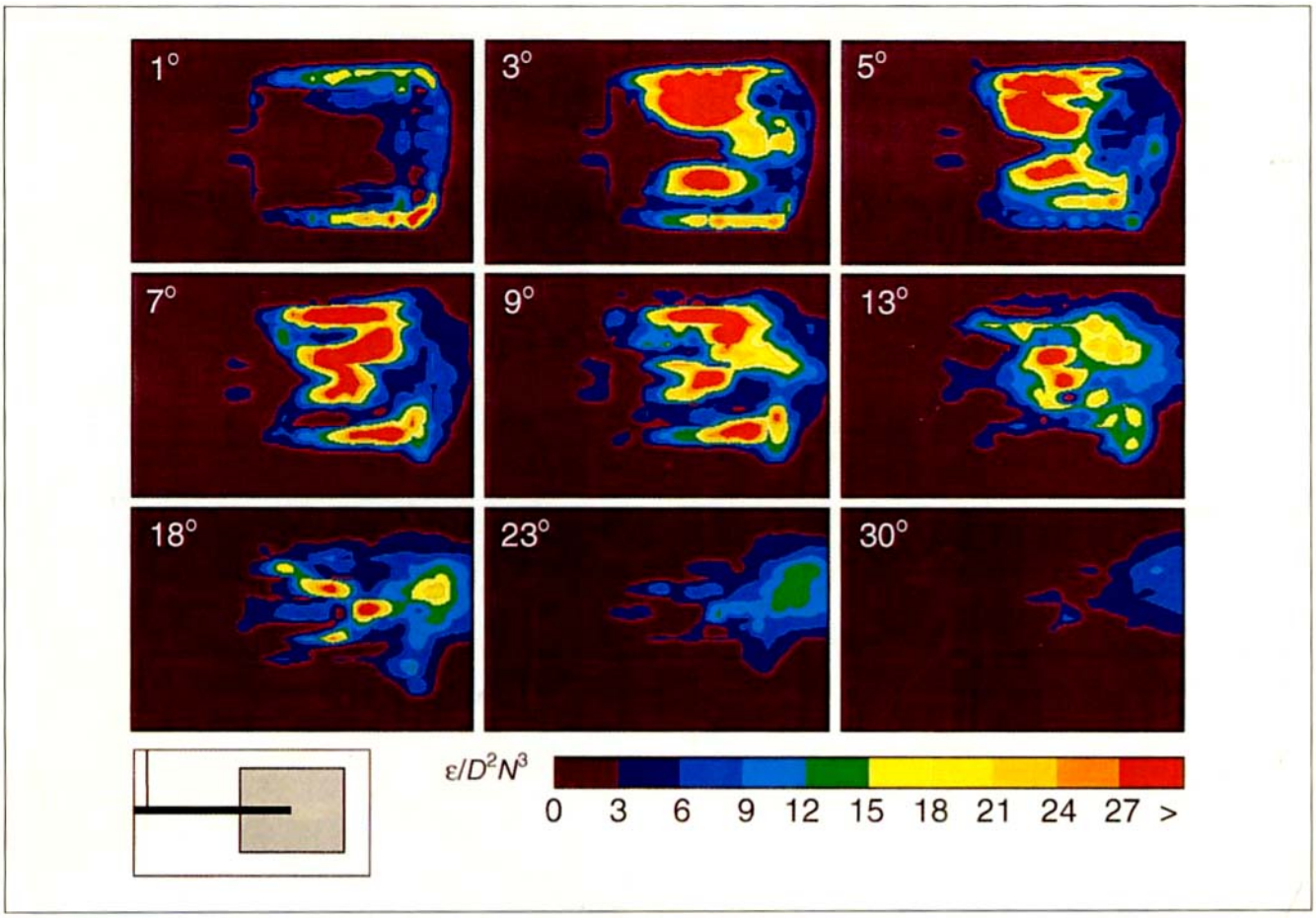


**Figure 12. Phase-resolved, averaged dissipation rate in the impeller-swept volume at various angles with respect to an impeller blade.**

strongest deviations observed are in the development of the impeller outflow. They are probably caused by not taking into account the presence of solid walls in the subgrid-scale model, and by a lack of spatial resolution.

Since the turbulent kinetic energy in the tank was well predicted, it is also worthwhile to study the energy dissipation rate, as predicted by the simulations. It appeared that the dissipation is very inhomogeneously distributed throughout the tank, with high levels in the impeller outflow region and low levels in the bulk. Furthermore, a detailed look at the dissipation rate in the impeller swept volume was presented. At the blade edges, and in the wake of the blades, high dissipation rates were encountered.

## Literature Cited

Bakker, R., "Micromixing in Chemical Reactors," PhD Thesis, Delft Univ. of Technology, Delft, The Netherlands (1996).

Dahm, W. J. A., K. B. Southerland, and K. A. Buch, "Direct, High Resolution, Four-Dimensional Measurements on the Fine Scale Structure of Sc ≫ 1 Molecular Mixing in Turbulent Flows," *Phys. Fluids A*, **3**(5), 1115 (1991).

Derksen, J. J., J. L. Kooman, and H. E. A. Van den Akker, "Parallel Fluid Flow Simulation by Means of a Lattice-Boltzmann Scheme," *Lect. Notes Comput. Sci.*, **1225**, 524 (1997).

Derksen, J. J., M. S. Doelman, and H. E. A. Van den Akker, "Three-Dimensional Phase-Resolved LDA Experiments in the Impeller Region of a Turbulently Stirred Tank," *Int. Symp. on Applications of Laser Techniques to Fluid Mechanics*, Lisbon (1998).

Distelhoff, M. F. W., J. Laker, A. J. Marquis, and J. M. Nouri, "The Application of a Strain Gauge Technique to the Measurements of the Power Characteristics of Five Impellers," *Exp. Fluids*, **20**, 56 (1995).

Eggels, J. G. M., "Direct and Large Eddy Simulation of Turbulent Flow in a Cylindrical Pipe Geometry," PhD Thesis, Delft Univ. of Technology, Delft, The Netherlands (1994).

Eggels, J. G. M., and J. A. Somers, "Numerical Simulation of Free Convective Flow Using the Lattice-Boltzmann Scheme," *Int. J. Heat Fluid Flow*, **16**, 357 (1995).

Eggels, J. G. M., "Direct and Large-Eddy Simulations of Turbulent Fluid Flow Using the Lattice-Boltzmann Scheme," *Int. J. Heat Fluid Flow*, **17**, 307 (1996).

Frisch, U., B. Hasslacher, and Y. Pomeau, "Lattice-Gas Automata for the Navier–Stokes Equation," *Phys. Rev. Lett.*, **56**(14), 1505 (1986).

Geist, A., A. Beguelin, J. Dongarra, W. Jiang, R. Manchek, and V. Sunderam, *PVM Parallel Virtual Machine*, The MIT Press, Cambridge, MA (1994).

Goldstein, D., R. Handler, and L. Sirovich, "Modeling a No-Slip Flow Boundary with an External Force Field," *J. Comput. Phys.*, **105**, 354 (1993).

Hinze, J. O., *Turbulence*, 2nd ed., McGraw-Hill, New York (1975).

Lee, K. C., and M. Yianneskis, "Turbulence Properties of the Impeller Stream of a Rushton Turbine," *AIChE J.*, **44**, 13 (1998).

Piomelli, U., P. Moin, and J. H. Ferziger, "Model Consistency in Large Eddy Simulation of Turbulent Channel Flows," *Phys. Fluids*, **31**, 1884 (1988).

Rushton, J. H., E. W. Costich, and H. J. Everett, "Power Characteristics of Mixing Impeller I and II," *Chem. Eng. Prog.*, **46**, 395, 467 (1950).
Schäfer, M., M. Yianneskis, P. Wächter, and F. Durst, "Trailing Vortices Around a 45° Pitched-Blade Impeller," *AIChE J.*, **44**(6), 1233 (1998).
Smagorinsky, J., "General Circulation Experiments with the Primitive Equations: 1. The Basic Experiment," *Mon. Weather Rev.*, **91**, 99 (1963).
Smoluchowski, M. von, "Versuch einer mathematischen Theorie der Koagulationskinetik koloïdaler Lösungen," *Z. Phys. Chem.*, **92**, 156 (1917).
Somers, J. A., "Direct Simulation of Fluid Flow with Cellular Automata and the Lattice-Boltzmann Equation," *Appl. Sci. Res.*, **51**, 127 (1993).
Stoots, C. M., and R. V. Calabrese, "Mean Velocity Field Relative to a Rushton Turbine Blade," *AIChE J.*, **41**, 1 (1995).
Van 't Riet, K., and J. M. Smith, "The Trailing Vortex System Produced by Rushton Turbine Agitators," *Chem. Eng. Sci.*, **30**, 1093 (1975).
Wu, H., and G. K. Patterson, "Laser-Doppler Measurements of Turbulent-Flow Parameters in a Stirred Mixer," *Chem. Eng. Sci.*, **44**(10), 2207 (1989).
Yianneskis, M., Z. Popiolek, and J. H. Whitelaw, "An Experimental Study of the Steady and Unsteady Flow Characteristics of Stirred Reactors," *J. Fluid Mech.*, **175**, 537 (1987).
Zhou, G., and S. M. Kresta, "Correlation of Mean Drop Size and Minimum Drop Size with the Turbulence Energy Dissipation and the Flow in an Agitated Tank," *Chem. Eng. Sci.*, **53**(11), 2063 (1998).

## Appendix: Symmetry Relations for the FCHC Lattice

The derivation of the dynamic equation (i.e., Eq. 9) from the differential form of the lattice–Boltzmann equation (i.e., Eq. 2) requires the application of some symmetry properties of the three-dimensional projection of the FCHC lattice. These properties are given in this Appendix, where $c_{i\alpha}$ is the component of the $i$th velocity vector $c_i$ (see Figure 2) in the (Cartesian) coordinate direction $\alpha$; $m_i$ is the multiplicity of the $i$th vector (see also Figure 2); and $\delta_{\alpha\beta}$ is the Kronecker delta-function:

$$\Sigma_i m_i = 24 \tag{A1}$$

$$\Sigma_i m_i c_{i\alpha} = 0 \tag{A2}$$

$$\Sigma_i m_i c_{i\alpha} c_{i\beta} = 12\,\delta_{\alpha\beta} \tag{A3}$$

$$\Sigma_i m_i c_{i\alpha} c_{i\beta} c_{i\gamma} = 0 \tag{A4}$$

$$\Sigma_i m_i c_{i\alpha} c_{i\beta} c_{i\gamma} c_{i\delta} = 4\delta_{\alpha\beta}\delta_{\gamma\delta} + 4\delta_{\alpha\gamma}\delta_{\beta\delta} + 4\delta_{\alpha\delta}\delta_{\beta\gamma}. \tag{A5}$$

*Manuscript received Aug. 24, 1998, and revision received Nov. 23, 1998.*